Competing Superior Electronic Structure and Complex Defect Chemistry in Quasi-One-Dimensional Antimony Chalcogenide Photovoltaic Absorbers

*Baiyu Zhang and Xiaofeng Qian**

Department of Materials Science and Engineering, Texas A&M University, College Station, Texas, 77843, USA

Department of Materials Science and Engineering, Texas A&M University, College Station, Texas, 77843, USA

Abstract: Antimony chalcogenides Sb_2Se_3 and Sb_2S_3 are an emerging class of quasi-one-dimensional van der Waals bonded materials with rapid progress and great promise for low-cost, high-efficiency, and scalable thin-film photovoltaics. Here using first-principles theoretical calculations, we show that antimony chalcogenides Sb_2Se_3 and Sb_2S_3 possess competing superior electronic structure and complex defect chemistry, limiting their photovoltaic performance. The high optical absorption, large Born effective charge, and high dielectric constant lead to low exciton binding energy and small hole effective mass, which ultimately benefit the photovoltaic performance. In contrast, quasi-1D antimony chalcogenides exhibit complex defect chemistry. The cation-anion antisites are the dominating native defects in Sb rich condition, while in Sb poor condition the anion-cation antisites are dominant. In both cases, the anion vacancies are also easy to form. These native defects introduce midgap transition levels which act as electron-hole recombination centers, limit the dopability, and lower the open circuit voltage. As a result, Sb_2Se_3 is a *p*-type semiconductor in Se rich condition, while Sb_2S_3 is an intrinsic semiconductor without significant free carrier density. Additionally, due to the unique quasi-1D structures and strong electron-lattice coupling, antimony chalcogenides are able to accommodate larger lattice relaxation than conventional 3D bulk crystals, resulting in negative-U behavior in their defect structures. Therefore, the competing superior electronic structure and complex defect chemistry suggest that, while antimony chalcogenides are excellent photoabsorbers, effort shall be made to suppress the formation of the detrimental native defects to further improve their open-circuit voltage, electronic transport, and thus power conversion efficiency.

Keywords: antimony chalcogenides, photovoltaics, density functional theory, defect chemistry, carrier concentration

1. Introduction

Photovoltaics (PV) convert solar energy to electricity and provide renewable and environment friendly energy. A variety of solar cells have been developed in the past using different absorbers, including silicon, cadmium telluride (CdTe), copper zinc tin sulfide (CZTS), copper-indium-gallium-selenium (CIGS), organic/polymer, and perovskite solar cells.[1-2] Among them, silicon-, CdTe- and CIGS-based solar cells are dominating the current commercial PV market. However, the current PV technologies still face some issues. For example, crystalline silicon (c-Si) solar cells suffer from high cost. The toxicity of Cd and the scarcity of Te are two notable issues of CdTe solar cell. The complexity of defect control hinders the further improvement of power conversion efficiency (PCE) in CZTS solar cell.[3] Perovskites have attracted tremendous attention in the last decade, and their PCE is approaching 25%,[4-5] making them promising for commercialization. Nevertheless, several challenges such as stability and toxicity of Pb-based perovskites need to be addressed.[6] Alternative stable, cost-effective and scalable PV absorbers are hence highly desired.

Recently, antimony chalcogenides (Sb_2X_3, where X=Se, S) have attracted great attention.[7] Sb_2X_3 possess quasi-one-dimensional (1D) ribbon-like structures, *i.e.* $(Sb_4X_6)_n$, which are bonded by weak van der Waals (vdW) interaction. Their suitable bandgaps (~1.2 eV for Sb_2Se_3, ~1.7 eV for Sb_2S_3), high optical absorption coefficient (~10^5 cm^{-1}), low cost, good stability, and earth abundant Sb and Se/S endow antimony chalcogenides with great potential in solar energy applications. Owing to the unique 1D vdW structures, antimony chalcogenides have benign grain boundaries with highly anisotropic transport property, very different from conventional bulk solar cell materials such as CdTe where the untreated grain boundaries often serve as carrier recombination centers and significantly limit the device performance. Different growth techniques have been

employed to improve samples with less defects and higher conductivity, and devices have been fabricated to suppress the interfacial diffusion and boost carrier separation, and improve stability and efficiency. Significant progress has been made on improving the device performance[8]. For example, a high PCE of 9.2% was recently achieved by using CSS technique by tuning Sb_2X_3 ribbons vertically aligned with the substrate.[9] Very recently, a record high PCE of 10% with antimony selenosulfide $Sb_2(S,Se)_3$ was achieved using an optimized hydrothermal deposition technique,[10] showing great promise of antimony chalcogenide based solar cells.

Defect tolerance is a crucial characteristic of excellent photovoltaic absorber. Native defects determine the carrier mobility, lifetime, recombination rate, and doping limit. Recently, it was theoretically predicted that Sb_2Se_3 is intrinsically *p*-type under Se-rich condition due to Se_{Sb} and even 2Se-on-Sb ($2Se_{Sb}$) antisites, and *n*-type under Sb-rich condition due to the low formation energies of donor defects such as V_{Se} and Sb_{Se} antisites.[11-12] Moreover, the defect formation energy calculations indicated that Se-on-Sb (Se_{Sb}) antisites with mid-gap transition levels were most likely to form, suggesting they may be the major obstacle to further improve the open-circuit voltage (V_{oc}).[13] Both calculations were conducted using first-principles density functional theory (DFT)[14-15] with HSE06 hybrid exchange-correlation energy functional[16] and D3 Grimme dispersion correction,[17] while different approaches were employed to correct the finite size effect on the charged defect formation energy calculations within the dilute defect limit. Besides the study of intrinsic defects, several possible dopants in Sb_2Se_3 were suggested to either enhance the native *p*-typeness or induce *n*-type doping[18]. Cai *et al*. pointed out that the compensation of the intrinsic donor and acceptor defects limit the electrical conductivity in Sb_2S_3 and proposed a two-step doping strategy to improve the efficiency.[19] These studies revealed that the native defects play critical roles in both Sb_2Se_3 and Sb_2S_3. Very recently, a deep level transient spectroscopy was

carried out to study deep level defects in Sb_2Se_3 and revealed the presence of traps in the 358-690 meV range below the conduction band edge, while the grain boundary is relatively benign.[20]

Using first-principles theoretical calculations, here we demonstrate that quasi-1D Sb_2Se_3 and Sb_2S_3 possess unique electronic structures and defect chemistry which eventually determines their superior optical and dielectric properties, and reveal their important implications on the photovoltaic performance as light absorbers. We further calculate the formation energies of a variety of intrinsic defects and defect transition levels in Sb_2X_3 and subsequently the equilibrium Fermi level, free carrier densities, and defect concentrations. Our results provide a theoretical interpretation of the observed *p*-type conductivity in Sb_2Se_3 and nearly intrinsic semiconductor behavior in Sb_2S_3. These theoretical findings not only offer microscopic understandings of the electronic structure and native defects in Sb_2X_3 photovoltaic absorber, but also may provide valuable guidance to further advance antimony chalcogenides based solar cells.

2. Methods

First-principles DFT calculations were performed using the Vienna Ab Initio Simulation Package (VASP).[21] We employed the Perdew-Burke-Ernzerhof (PBE)[22] form of exchange-correlation energy functional within the generalized gradient approximation (GGA)[23] and a Γ-centered Monkhorst-Pack[24] k-point sampling for Brillouin zone integration. A plane wave basis set with a 400eV energy cutoff and a 4×4×12 k-point grid were used for structure optimization and electronic relaxation. As DFT-GGA often underestimates the band gap, we applied the modified Becke-Johnson (MBJ) [25-26] exchange potential for electronic structure and optical property calculations. Frequency dependent dielectric function was calculated in the independent particle approximation with a dense k-point sampling of 10×10×30. The convergence criteria for

electronic relaxation was set to 10-6 eV, and the maximal residual force for structure optimization was less than 0.01 eV $Å^{-1}$.

As the accuracy of formation energies is important for defect calculations, we employed the HSE06 hybrid exchange-correlation functional to further relax bulk and defect structures and calculate the total energies. This approach was previously shown to provide accurate prediction for the atomic and electronic structures in defective systems.[27-28] Savory *et al*. and Huang *et al*. also reported that the DFT calculations with HSE06 functional reproduce the experimental lattice constants and electronic bandgap of Sb_2Se_3.[11, 13] Different vdW corrections were tested and compared, including optB86-vdW non-local correlation functional[29-31] and D3 dispersion correction.[17] The obtained lattice constants from HSE06-D3 are in good agreement with the experiment data, and the difference of the lattice constants calculated from different functionals is minimal. Therefore, we used HSE06-D3 for all defect calculations with a supercell of 1×1×3 containing 60 atoms for both Sb_2Se_3 and Sb_2S_3 to mimic the dilute defect limit. Additionally, spin polarization was considered in order to deal with unpaired electrons.

3. Results and discussions

3.1. Crystal and electronic structure of quasi-1D antimony chalcogenides. Antimony chalcogenides (Space group: Pnma, #62), *i.e*. Sb_2Se_3 and Sb_2S_3, possess a unique structure with infinite quais-1D ribbons, where the ribbons are stacked by vdW interaction, as shown in **Figure 1a-1c**. Their ground state structures are formed by quasi-1D ribbons which are weakly bonded by vdW interaction while within the ribbon Sb-Se/S are bonded by strong valence bonds, forming infinite one-dimensional ribbons (*i.e*. $(Sb_4X_6)_n$). The unit cell contains 20 atoms, where there are three symmetry-inequivalent types of Se/S atoms and two symmetry-inequivalent types of Sb, as indicated in **Figure 1a and 1b**. **Table S1** summarizes the lattice parameters calculated by DFT

with different exchange-correlation energy functionals, as compared to experimental values. The obtained lattice constants from HSE06-D3 are in good agreement with the experiment data, and the difference of the lattice constants calculated from different functionals is minimal. Thus, all the following DFT calculations including electronic and optical properties and defect calculations were carried out with the HSE06-D3 relaxed structures.

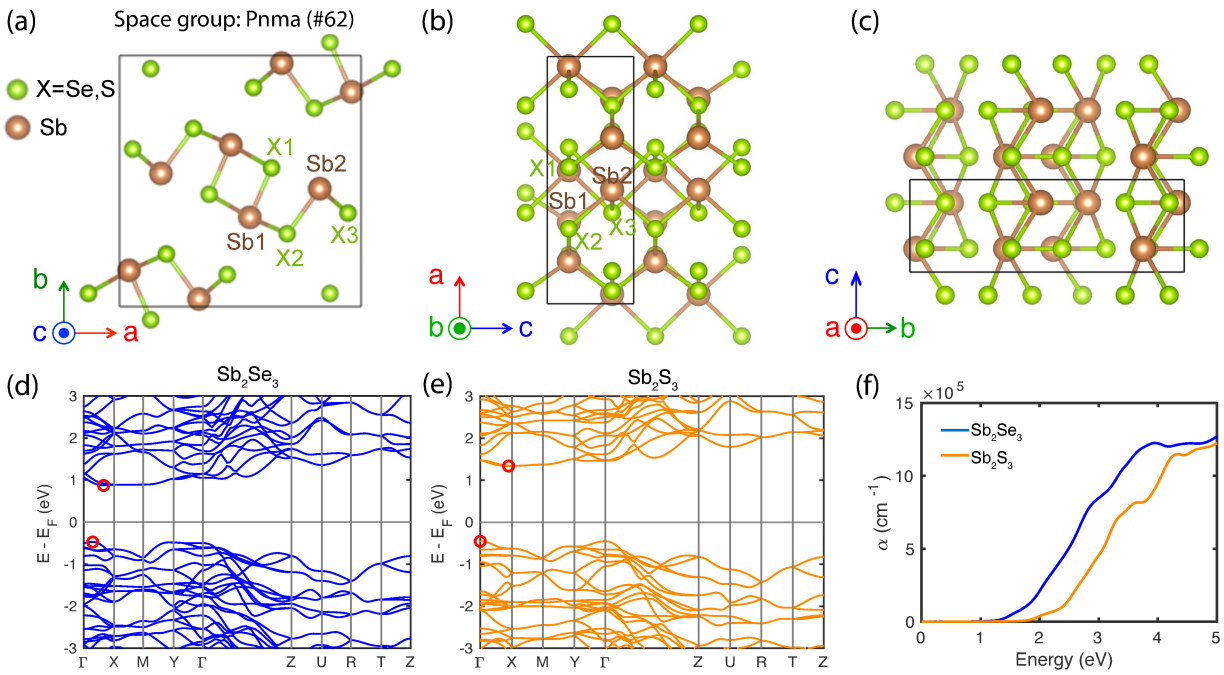

Figure 1. (a-c) Crystal structure of antimony chalcogenides Sb_2Se_3 and Sb_2S_3 with space group Pnma from three different view angles. The quasi-1D $(Sb_4Se_6)_n$ ribbons are along the c direction, while the ribbons are bonded by van der Waals interaction along a and b directions. (d) and (e) Calculated electronic band structures of Sb_2Se_3 and Sb_2S_3. Red circles indicate VBM and CBM. (f) Calculated optical absorption spectra.

The electronic band structures of Sb_2Se_3 and Sb_2S_3 along the high symmetry points in the Brillouin zone are shown in **Figure 1d** and **1e**. As DFT-PBE often underestimates band gap and

DFT-HSE06 calculations are usually expensive, we compute the band structures along the full k-paths by using the modified Becke-Johnson (MBJ) exchange potential functional[25-26] which is known to provide accurate electronic structures comparable to hybrid functional and many-body perturbation theory with GW approximation. The electronic bands of Sb_2Se_3 and Sb_2S_3 along ΓZ are more dispersed than those along ΓY and ΓX, indicating the higher group velocity and more facile electron transport along the ribbons (*c* axis) than across ribbons (*a*/*b* axes). Moreover, the MBJ and HSE06 calculated bandgaps of Sb_2Se_3 and Sb_2S_3 are summarized in **Table S2**. Both Sb_2Se_3 and Sb_2S_3 have indirect gaps located along ΓX. The calculated band gaps in Sb_2Se_3 and Sb_2S_3 are 1.35 and 1.79 eV, respectively, making them good photovoltaic absorber candidates. The results are in reasonable agreement with GW quasiparticle bandgap (1.3 eV for Sb_2Se_3, and 1.5 eV for Sb_2S_3).[32] We further investigated the spin-orbit coupling (SOC) effect on the band structure. The results are shown in Figure S1, where the band structures are very similar to each other in both Sb_2Se_3 and Sb_2S_3 cases. The change in the bandgap is also minimal (< 0.1 eV for both Sb_2S_3 and Sb_2Se_3). Moreover, SOC induced splitting is more significant for higher conduction bands, and much less on the low energy conduction bands and valence bands. Therefore, unlike perovskite materials such as $CsPbBr_3$ *etc*. where SOC induced band energy change can be as large as 1 eV, the spin-orbit coupling effect in Sb_2S_3 and Sb_2Se_3 is small, hence the SOC was not included in the defect calculations.

Furthermore, small electron/hole effective mass (e.g. < 0.5 m_0, where m_0 is the free electron mass) is often beneficial for carrier transport.[33-34] We calculate anisotropic electron and hole effective masses using a parabolic fitting at the CBM and VBM, and the results are presented in Table S3 and Table S4. The calculated hole effective masses of Sb_2Se_3 and Sb_2S_3 are small, with

the value of 0.42 m_0 and 0.56 m_0 along x, and 0.52 m_0 and 0.41 m_0 along z, which are desired for *p*-type semiconductors..

3.2. Anisotropic dielectric properties of quasi-1D antimony chalcogenides. Besides the suitable electronic band gap and small hole effective mass, the dielectric constant of Sb2X3 is quite large. A large dielectric constant usually leads to strong screening to charges and defects, thereby suppressing carrier scattering and recombination. Typically the macroscopic dielectric constant of 10 or higher, including the electronic and ionic contributions, will enhance electron-hole pair dissociation, or exciton dissociation into free charge carriers in photovoltaics.[33, 35] The electronic contribution comes from the polarization by redistribution of electronic density, while the ionic part is associated with the polarization by ionic motion. The calculated dielectric tensors for Sb_2Se_3 and Sb_2S_3 are summarized in **Table 1**, where the electronic part is computed using the HSE06 functional since it is sensitive to the band gap. The dielectric tensors of both compounds show significant anisotropy where both ionic and electronic contributions in the dielectric constants along z (ribbon) and x directions are higher than that along y. The large dielectric constants of Sb_2X_3 indicate that the charge carriers are subject to enhanced screening when transporting along the ribbons, thereby reducing carrier scattering and recombination.

Table 1. Dielectric constants along three principal directions. Ionic and electronic contributions are calculated using DFT-PBE and DFT-HSE06 functionals, respectively.

materials	direction	ε_{ion}	ε_{elec}
Sb_2Se_3	xx	97.56	15.43
	yy	3.94	10.69
	zz	76.97	15.46
Sb_2S_3	xx	66.08	11.06
	yy	4.025	8.28
	zz	90.39	11.63

To understand the large dielectric constants in Sb_2X_3, we further investigate the corresponding Born effective charge (BEC). The BEC tensors of symmetry-inequivalent Sb and Se/S atoms are calculated using DFT-PBE. The results are listed in **Table S5**. The valence of Sb and Se/S elements are +3 and -2. However, in Sb_2Se_3, the ions present a maximum effective charge of +7.22 e on Sb1, +7.49 e on Sb2, -4.19 e on Se1, -4.01 e on Se2, and -4.93 e on Se3, much higher than their nominal ionic charges. A similar trend was also observed in Sb_2S_3, with the BEC of 6.86 e on Sb1, 6.38 e on Sb2, -3.86 e on S1, -3.75 e on S2, and -4.59 e on S3. The BEC represents the change in the electric polarization upon atom displacement. For ideal ionic crystals with complete charge transfer, the BEC would be the same as the nominal ionic charge (*e.g.*, +3 for Sb and -2 for Se and S). However, the BEC for xx and zz component in Sb_2Se_3 and Sb_2Se_3 are much higher than the nominal charge, indicating that their bonding nature is more complex than the ideal ionic bond and the electrons shared via covalent bonding may significantly redistribute upon atomic displacement and contribute to the polarization change.

Low exciton binding energy for efficient electron-hole separation. Based on the effective mass and dielectric constant, we can estimate the exciton binding energy E_b using hydrogenic model: $E_b = \frac{\mu}{m_0\epsilon^2} R_H$, where R_H is the Rydberg constant of hydrogen atom (13.6 eV), and ϵ is the average dielectric constant. μ is the effective reduced mass of the exciton, obtained by $\frac{1}{\mu} = \frac{1}{m_h^*} + \frac{1}{m_e^*}$. Since antimony chalcogenides exhibit structural anisotropy, we calculate the anisotropic binding energy based on their anisotropic effective mass (Table S3 and S4). The calculated effective reduced exciton mass can be as small as 0.23 m_0 and 0.39 m_0 for Sb_2Se_3 and Sb_2S_3, respectively. Consequently, the exciton binding energy is as low as 12.9 meV and 39.4 meV, comparable with the thermal energy (*i.e.* k_BT, 25 meV at room temperature). The low exciton

binding energy suggests efficient dissociation of photoexcited electron and hole pairs into free carriers. Finally, we also calculated another important physical property for photovoltaic absorber, *i.e.* optical absorption spectra of Sb_2X_3 using DFT-MBJ. The frequency-dependent averaged optical absorption coefficient is shown in **Figure 1f**, and the calculated values agree with the experimental data of 10^4~10^5 cm^{-1} for Sb_2S_3 and >10^5 cm^{-1} for Sb_2Se_3 in the visible region[36], demonstrating antimony chalcogenides are indeed good solar absorbers.

The above theoretical investigations of electronic, optical, and dielectric properties show that Sb_2Se_3 and Sb_2S_3 have several nice characteristics, including suitable bandgap, small effective hole mass, small exciton binding energy, large dielectric constants, hence strong screening, and high optical absorption coefficient, endowing Sb_2Se_3 and Sb_2S_3 with great potential as light absorbers in thin-film PV devices.

3.3. Complex point defect chemistry in quasi-1D antimony chalcogenides. Experiments have shown that Sb_2X_3 solar cells suffer from low open-circuit voltage (V_{oc}), which is often caused by high recombination rate due to the mid-gap trap states.[37] In order to understand the types of defects that may generate mid-gap levels, we conduct a study of intrinsic point defects of Sb_2X_3. Here we consider five types of intrinsic defects, namely vacancy ($V_{Sb,}$ $V_{Se/S}$), interstitial (S_i, Se_i, and Sb_i), and Sb and Se/S antisites (Sb_S and Se_{Sb}/S_{Sb}) for all symmetry-inequivalent atomic sites with different charge states.

The formation energy of charged defect is defined as,[38]

$$\Delta E^f(D,q) = E(D,q) - E(bulk) - \Sigma n_i \mu_i + q\epsilon_F + E_{corr}, \quad (1)$$

where $E(bulk)$ and $E(D,q)$ are the total energy of the pristine host cell and the supercell with defect D in the charge state q, respectively. μ_i refers to the chemical potential of atomic species i, and n_i is the number of atoms added ($n_i > 0$) or removed ($n_i < 0$). $q\epsilon_F$ represents the chemical

potential of electron reservoir, where ϵ_F is the Fermi level. ϵ_F is conventionally referenced to the valence band maximum (VBM) in the perfect cell and varies between the VBM and conduction band minimum (CBM). The chemical potential corresponds to the energy of exchanging atoms between the defect and the element reservoir. μ_i can be split into two parts as $\mu_i = \mu_i^o + \Delta\mu_i$. μ_i^o represents the chemical potential of the reference, associated with the elemental phases of each species, and $\Delta\mu_i$ is the allowed chemical potential variation. $\Delta\mu_i$ is determined by the rule that Sb_2X_3 must be more stable than any other competing phase. In the calculations, we only consider two extreme cases, i.e. the X rich (Sb poor) and X poor (Sb rich) condition. We therefore have the following set of constraints on $\Delta\mu_{Sb}$ and $\Delta\mu_{Se/S}$: $\Delta\mu_{Sb} < 0$, $\Delta\mu_{Se/S} < 0$, and $2\Delta\mu_{Sb} + 3\Delta\mu_{Se/S} = \Delta\mu_{Sb_2Se_3}$. E_{corr} is a correction to the formation energy to account for the spurious image charge interaction due to the finite supercell formalism for simulating the dilute defect limit. Specifically, E_{corr} addresses two issues: (1) the interaction among the defect and its images under periodic boundary condition, and (2) the electrostatic potential alignment between the defect supercell and the pristine bulk.[39] Freysoldt et al. developed a correction method which treats the long-range and short-range interactions between charged defects separately[40] where an isotropic dielectric constant was used. Kumagai and Oba extended this method to anisotropic systems by using full dielectric tensor[41]. Given the high anisotropic Sb_2X_3, we adopt the correction method proposed by Kumagai et al. To verify if this correction scheme is efficient for correcting the defect formation energy of our materials, we further calculate the formation energy with and without the correction using PBE functional (Figure S2). The finite size correction indeed plays a critical role in determining the formation energy of charged defects in dilute limit, as the relative energy with and without the correction can differ significantly, especially for the small supercell of 1×1×3. And this correction decreases in a larger supercell. In general, the relative energies with the correction of 1×1×3

supercell are close to those of 2×2×6. Therefore, considering the high computational cost of hybrid functional for large supercell, we choose the supercell of 1×1×3 and apply the finite size correction to the defect formation energy.

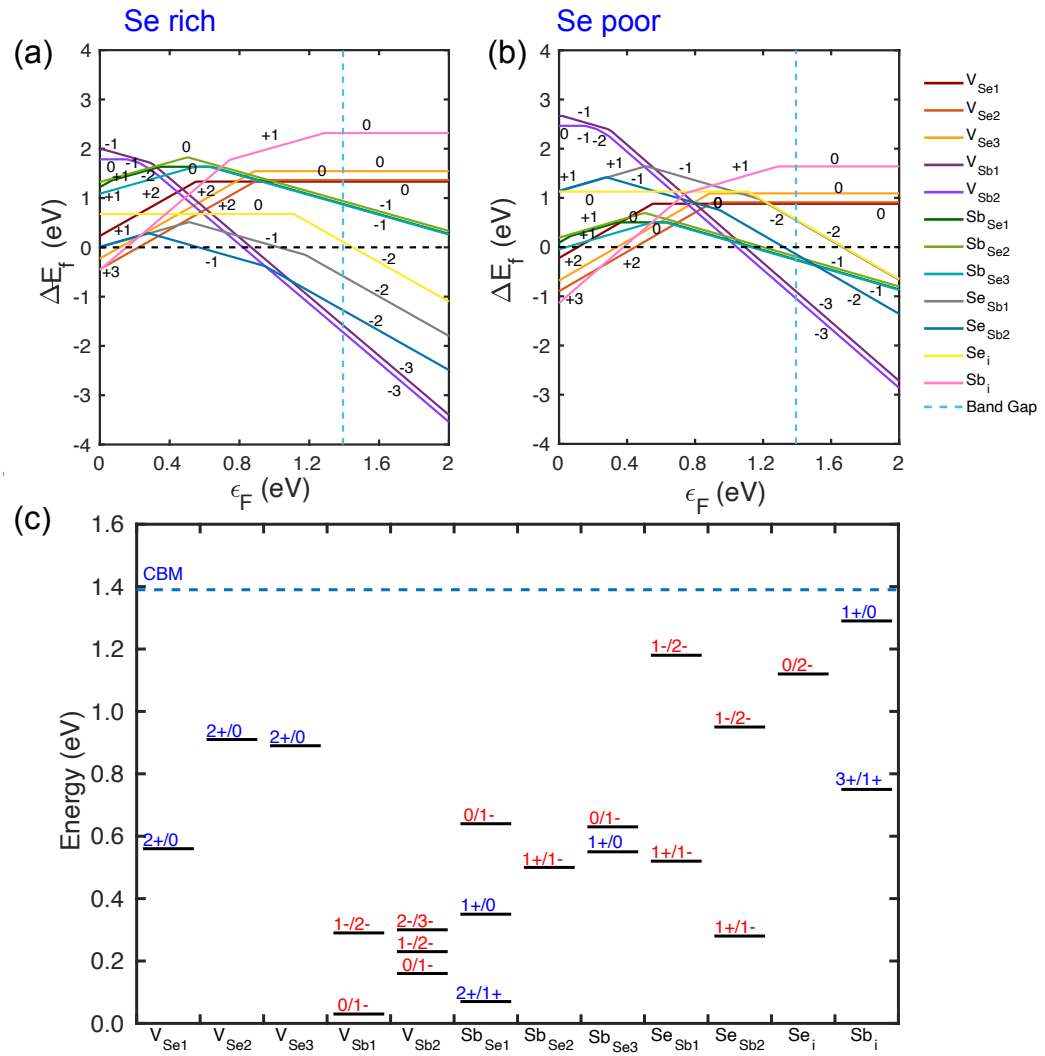

Figure 2. Defect formation energy diagrams of Sb_2Se_3 under (a) Se rich and (b) Se poor condition. (c) Defect transition levels in Sb_2Se_3. The formation energies of native point defects in Sb_2Se_3 is plotted as a function of the Fermi level with VBM as reference. The bandgap adopted here is calculated by HSE06. The slope of each line indicates the most favorable charge state at the corresponding Fermi level. Positive and negative charge state indicate the donor and acceptor,

respectively. The red and blue colors in (c) indicate the donor and acceptor transition levels, respectively.

The formation energy of charged defects can be further used to compute defect transition level, $\epsilon(q/q')$, It is defined as the Fermi level for which the formation energy of a charge state q is equal to the formation energy of a charge state q', indicating the relative stability of defect in charge state q. It is given by $\epsilon(q/q') = \frac{E_f^{D,q}(E_F=0)-E_f^{D,q'}(E_F=0)}{q'-q}$. Shallow transition levels located near the band edges are associated with n- or p-type doping, while deep transition levels usually act as carrier recombination centers, referred as trap states. These are the transition levels in thermodynamic equilibrium where atoms and electrons in defect systems are fully relaxed to their equilibrium state, different from the transition levels upon optical absorption.[42]

We first investigate the intrinsic defects of Sb_2Se_3. Due to the anisotropic structure, defects behave differently at symmetry-inequivalent sites. The formation energy as a function of the Fermi level (E_F) is plotted in **Figure 2a** and **2b** for Se rich and Se poor conditions, respectively. The antisite (Se_{Sb1}, Se_{Sb2}, Sb_{Se1}, Sb_{Se2}, and Sb_{Se3}) and interstitial (Se_i and Sb_i) defects are likely to act as donors/acceptors depending on the Fermi level. When the Fermi level is near VBM, those defects donate electrons and exhibit positive charge states. When the Fermi level is close to CBM, they accept electrons and are negatively charged. The formation of defects can be regulated by controlling the chemical potentials of the associated elements. In Se rich condition, acceptor-like defects V_{Se2} and V_{Se3} have negative formation energy when the Fermi level is located at VBM (*i.e.* $E_F = 0$). In addition, when $E_F = 0$, Sb interstitials also have low formation energie, and Se_{Sb1}, and Se_{Sb2} have formation energy close to zero. Therefore, when the Fermi level is close to VBM, the Se vacancies, Sb interstitials, and Se_{Sb} antisite defects are the dominant defects in Se rich

condition. As shown in **Figure 2c**, those defects create mid-gap trap states. As E_F increases, V_{Sb} becomes more likely to form due to the decrease of its formation energy. Among all the defects, when the Fermi level is close to VBM, the donor defect V_{Se2} with charge state q=+2 has the lowest formation energy, contributing free electrons to the conduction bands and making it *n*-type. On the other hand, when the Fermi level is close to CBM, the acceptor defect Se_{Sb2} with charge state q=-1 and V_{Sb} with charge state q=-3 have the lowest formation energies, donating free holes to the valence bands and making the system *p*-type. V_{Se2} (q=+2) and Se_{Sb2} (q=-1) have the same formation energy at $E_F = 0.4\ eV$ under Se-rich condition. Thus, the Fermi level will be pinned at around 0.4 eV. Under Se-poor condition, Sb_{Se}, V_{Se} and Sb_i have even lower formation energy while V_{Sb}, Se_{Sb} and Se_i have higher formation energy at $E_F = 0\ eV$, compared wth Se rich condition. The easier formation of the hole killers will restrain the free carriers in the *p*-type Sb_2Se_3. Therefore, Se rich condition is recommended during growth. The Fermi level in this case is pinned at around 0.7 eV by donor defect V_{Se2} and acceptor defect Sb_{Se1}. Despite the use of different energy correction and consequently slightly different defect formation energies, both our study and previous works[11, 13] on defect chemistry of Sb_2Se_3 reveal the deep level trap states produced by the defects V_{Se}, Se_{Sb} and Se_i in Se rich condition, and the detrimental donor defect V_{Se} has even lower formation energy in Se poor condition. In the work by Huang *et al.*, they also demonstrated the pinned Fermi level at around 0.4 eV in *p*-type Sb_2Se_3.[11] Indeed, in a recent experimental study[43] the deep-level transient spectroscopy (DLTS) measurements indicate the presence of hole trap states located at 0.48 ± 0.07 eV and 0.49 ± 0.03 eV for vapor transport deposition (VTD) and rapid thermal evaporation (RTE) fabricated samples. Based on our calculated defect transition levels, the hole trap state is highly likely to be caused by V_{Se}. The DLTS study also implies an electron trap state lying at 0.61 ± 0.03

eV and 0.6 $\pm$ 0.02 eV for VTD and RTE fabricated samples, which is possibly a consequence of the formation of acceptor defect Se_{Sb}.

Sb_2S_3 exhibits the similar behavior as Sb_2Se_3, as shown in **Figure 3a-c**. The antisite (S_{Sb1}, S_{Sb2}, Sb_{S1}, Sb_{S2}, and Sb_{S3}) defects possess positive charge states when the Fermi energy moves towards VBM, while they exhibit accept-like defects with negative charges as Fermi energy is close to CBM. V_{S2}, V_{S3}, Sb_i, S_{Sb2} and S_{Sb1} are dominant defects with negative formation energy at $E_F = 0$ under S-rich condition. S-on-Sb antisites possess low formation energy, suggesting antisite defects in Sb_2S_3 are easy to form in the quasi-1D structure. The Sb-on-S antisites can be more easily to form under S poor conditions. Comparing the formation energies under two extreme conditions, the donor defect concentration is higher under S poor condition, due to the significant decrease of the formation energy of Sb-on-S antisites, Sb interstitials and S vacancies. Those defects will be detrimental to the free carrier concentration and trap the carriers. Indeed, a recent DLTS study demonstrates the deep-level electron trap states ~ 0.6-0.7 eV below the CBM in Sb rich condition, which can be well assigned to V_S.[44] The Fermi levels are pinned at 0.75 eV by S_{Sb2} (q=+1) and V_{Sb2} (q=-3) in S rich condition, and at 0.85 eV by V_{S2} (q=+2) and V_{Sb2} (q=-3) in S poor condition. The calculated formation energies are consistent with the recent work by Cai *et al.*,[19] and further confirm the low device efficiency of Sb_2S_3 solar cells is caused by the formation of donor defect sulfur vacancies, and *p*-type doping in Sb_2S_3 is limited due to the Fermi level pinning far away from the VBM.

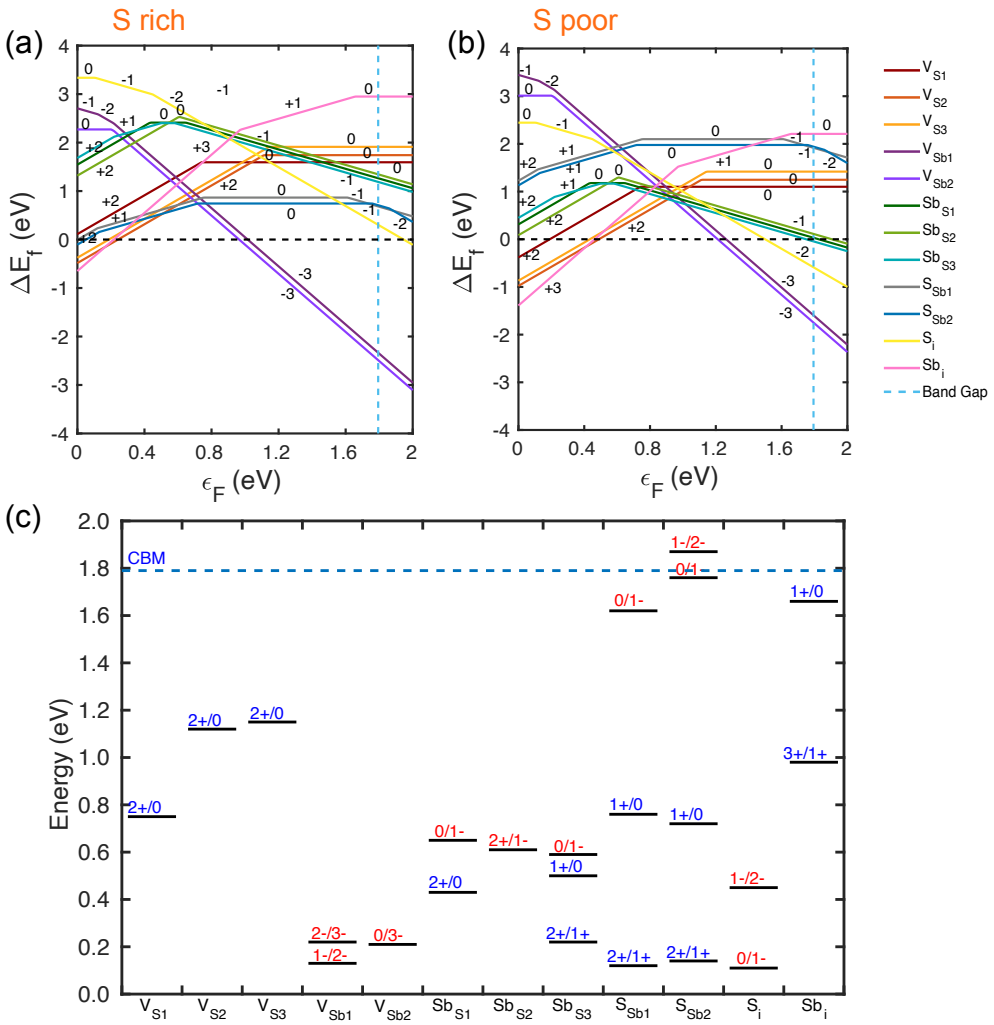

Figure 3. Defect formation energy diagrams of Sb_2S_3 under (a) S rich and (b) S poor condition. (c) Defect transition levels in Sb_2S_3. The formation energies of native point defects in Sb_2S_3 is plotted as a function of the Fermi level with VBM as reference. The bandgap adopted here is calculated by HSE06. The red and blue colors in (c) indicate the donor and acceptor transition levels, respectively.

To further increase the carrier density of Sb_2X_3, extrinsic doping is a feasible approach. We then investigate the dopability of Sb_2Se_3 and Sb_2S_3. Dopability refers to the domain of the Fermi energy accessible through doping [45]. When acceptor-like defects are doped into the system, the Fermi

energy is shifted towards the valence band, and the acceptor formation energy decreases with ϵ_F. With increasing hole doping, the Fermi energy will decrease and shift towards VBM. Subsequently the formation energy of hole killers will also decrease, and at certain point they will form spontaneously. Across this point, further doping is inhibited because the formation of the hole killers (e.g. V_{Se2}^{+2}) will negate the acceptors. As mentioned above, the doping limit of Sb_2Se_3 occurs at 0.4 eV and 0.7 eV for Se-rich and Se-poor growth conditions, respectively, and the doping limit of Sb_2S_3 occurs at 0.75 eV and 0.85 eV for S-rich and S-poor growth conditions, respectively. The Se/S-rich condition destabilizes the donor defects (hole killers), hence facilitate *p*-type doping. Hence, Sb_2Se_3 has better *p*-type doping capability than Sb_2S_3, and the doping limit can be further overcome by passivating the killer defects.

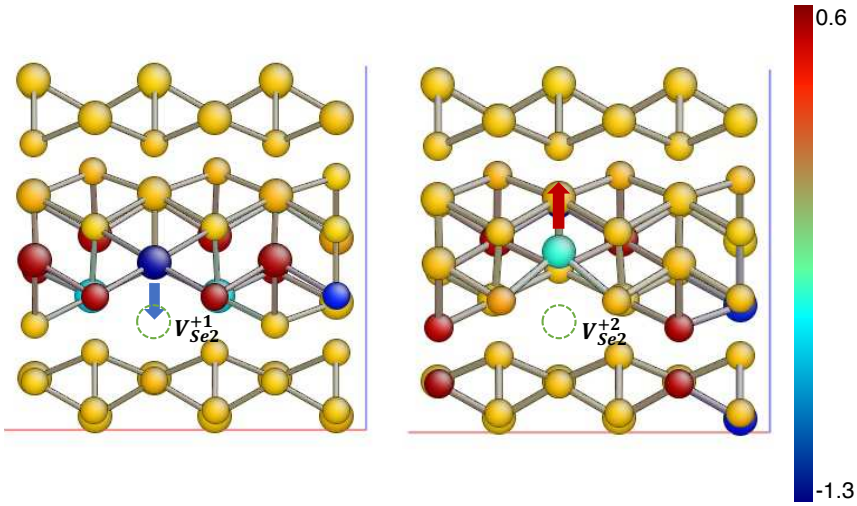

Figure 4. Atomic structures of V_{Se2}^{+1} and V_{Se2}^{+2}. The color of the atoms indicates the electron depletion (blue) or accumulation (red) with respect to V_{Se2}^{0} and V_{Se2}^{+1}, respectively.

Some of the defects exhibit negative U behavior[46-47]. For example, V_{Se} and V_S with +1 charge state are unstable at any value of the Fermi level. Its formation energy is always higher than that of 0 and +2 charge states. This character is related to strong electron-lattice interaction, which

leads to significant atomic relaxation. **Figure 4** illustrates the local lattice relaxations of V_{Se2} with +1 and +2 charge states, *i.e.* V_{Se2}^{+1} and V_{Se2}^{+2}, and the color of the atoms represents charge transfer with respect to V_{Se2}^{0} and V_{Se2}^{+1}, respectively, obtained from Bader charge analysis[48]. The formation of +2 charge state, V_{Se2}^{+2}, is accompanied by a large outward relaxation away from Se vacancy. In fact, the nearest-neighbor Sb atoms relax away from the vacancy by -19%, -5% and 21% of the equilibrium V_{Se2}-Sb bond length (*i.e.* the bond between Se vacancy and its nearest Sb atom) for the +0, +1, and +2 charge states with respect to the Se-Sb bond length in the pristine bulk. The released energy due to large local lattice relaxation overcompensates the electron Coulombic interaction energy. Since antimony chalcogenides have soft quasi-1D ribbon-like structures with weak interchain interaction, they are able to accommodate larger lattice relaxation than conventional 3D bulk crystals, thereby exhibiting negative U behavior in these defect structures.

3.4. Defect concentration, carrier density and their implication on p-/n-typeness. Based on the defect formation energy calculated above, the equilibrium Fermi level at a given temperature, charged defect concentration and carrier density are obtained by solving a set of self-consistent equations under charge neutrality [49]. Assuming the entropy and pressure contributions to the Gibbs free energy are negligible, then the defect concentration in charge state q is given by

$$c_{D,q}(E_F, T) = N_{site} \mathrm{e}^{-\frac{E_f^{D,q}(E_F)}{k_B T}}, \tag{2}$$

where N_{site} is the number of sites per volume available for defect D with charge state q, and k_B is the Boltzmann constant. The concentration in this case is determined by the Fermi level E_F and the synthesis temperature T. The charge neutrality condition yields

$$-n_e(E_F, T) + n_h(E_F, T) + \sum_D \sum_q q_D \cdot c_{D,q}(E_F, T) = 0 \tag{3}$$

n_e and n_h are free electron and hole concentrations. n_e and n_h can be calculated by integrating the product of electron/hole density of states (DOS) and electron/hole Fermi-Dirac distribution function,

$$n_e(E_F,T) = \int_{CBM}^{+\infty} g_e(E) f(E-E_F,T)dE, \tag{4}$$

$$n_h(E_F,T) = \int_{-\infty}^{VBM} g_h(E)\big(1-f(E-E_F,T)\big)dE. \tag{5}$$

$f(E-E_F,T)$ is the Fermi-Dirac distribution. $g_e(E)$ and $g_h(E)$ are the DOS of electrons and holes, respectively, which are approximated as $g_{e,h} = \frac{1}{4\pi^2}\left(\frac{2m_{e,h}^*}{\hbar^2}\right)^{\frac{3}{2}}\sqrt{E}$. $m_{e,h}^*$ are the electron and hole effective masses and can be obtained from the curvature of band energy at CBM and VBM, where $m_{e,h}^* = \left(\frac{1}{\hbar^2}\frac{\partial^2 E_{e,h}(\boldsymbol{k})}{\partial^2 \boldsymbol{k}}\right)^{-1}$.

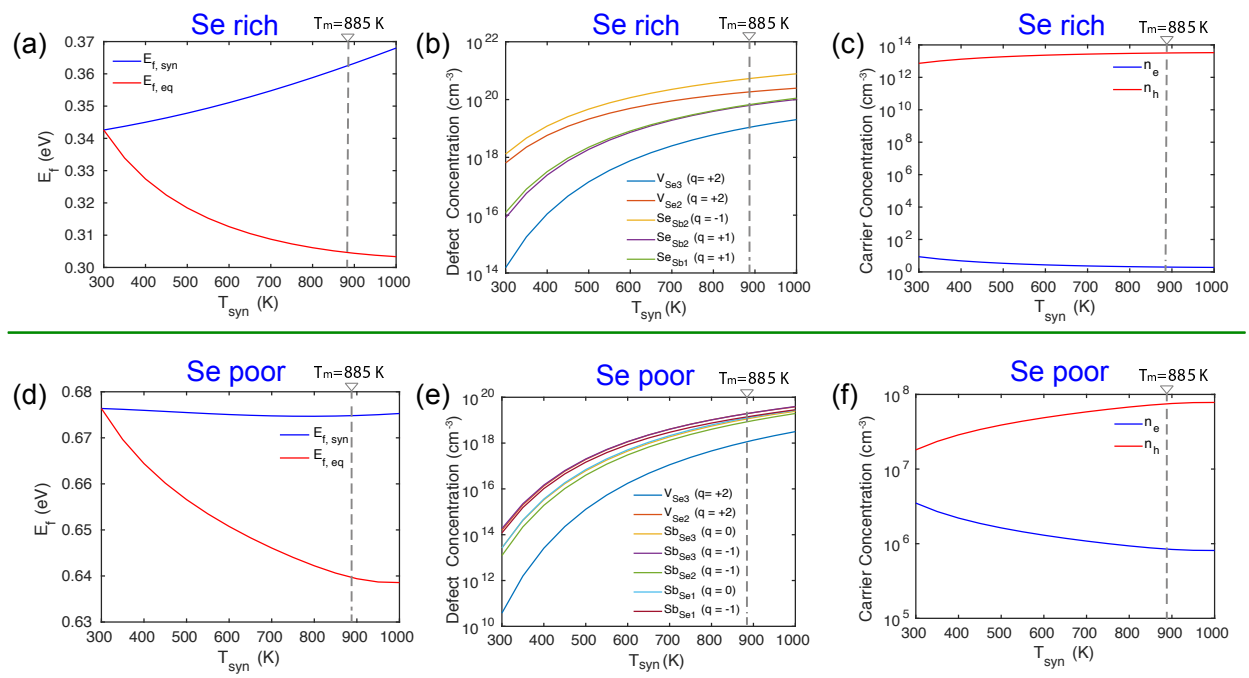

Figure 5. (a) and (c) Fermi level of Sb_2Se_3 at synthesis and equilibrium temperatures as a function of synthesis temperature under Se rich and Se poor conditions, respectively. (b) and (e) Electron and hole densities at equilibrium temperature as a function of synthesis temperature under Se rich

and Se poor conditions, respectively. (c) and (f) The concentration of dominant defects as a function of synthesis temperature under Se rich and Se poor conditions, respectively. The dashed line indicates the melting temperature of Sb_2Se_3 at 885 K.

For a given chemical potential and synthesis temperature, the Fermi level at equilibrium, defect concentrations, and carrier densities are determined as the self-consistent solution to the above equations (eqs 2-5). Moreover, as the synthesis temperature is often different from operating temperature, we also calculate the corresponding values at room temperature (*i.e.* 300K in the present work) by assuming that the defect concentrations remain the same and only the charge state of defects will re-equilibrate under the dilute limit. In this case, the densities of different charge states of the same defect type redistribute by following Boltzmann statistics.

Using the method described above, we first calculate the carrier density and defect concentrations in Sb_2Se_3. **Figure 5a** and **5d** show the Fermi level under synthesis temperature ($E_{F,\mathrm{syn}}$) and equilibrium temperature ($E_{F,\mathrm{eq}}$) as a function of synthesis temperature from 300 to 1000 K. The melting temperature of Sb_2Se_3 is 885 K, below 1000K, as indicated by the dashed line in **Figure 5**. The corresponding Fermi level is calculated by assuming the system is quenched from synthesis temperature to room temperature, and during annealing the defect concentrations remain the same but the charge state of each defect type can change and re-equilibrate. The calculated $E_{F,\mathrm{eq}}$ decreases as temperature increases. Under Se rich condition, the equilibrium Fermi level is around 0.3-0.34 eV within the synthesis temperature range, which is close to VBM, showing a *p*-type nature. The dominant carrier is hole, as shown in **Figure 5c**, with the concentration on the order of 10^{13} cm^{-3}, in agreement with the experiment (in the order of ~10^{14} cm^{-3}),[50] which is majorly contributed by the dominant defect Se_{Sb1}^{-1} (**Figure 5b**). In Se-poor condition, the equilibrium Fermi level is located near the half of the bandgap, suggesting the weak *p*-typeness and low hole density.

It is attributed to the formation of donor defects V_{Se2}^{+2} and V_{Se3}^{+2}, although there is still high concentration of acceptor defects Sb_{Se1}^{-1} and Sb_{Se3}^{-1}, as shown in **Figure 5e**. **Figure 5f** shows the calculated the hole and electron density. The hole density is only on the order of 10^7 cm^{-3} and increases with the temperature. The electron density is on the order of 10^6 cm^{-3} and decreases with the temperature. Our calculations therefore confirm that Sb_2Se_3 is an intrinsic *p*-type semiconductor, and the Se-rich growth condition is desired.

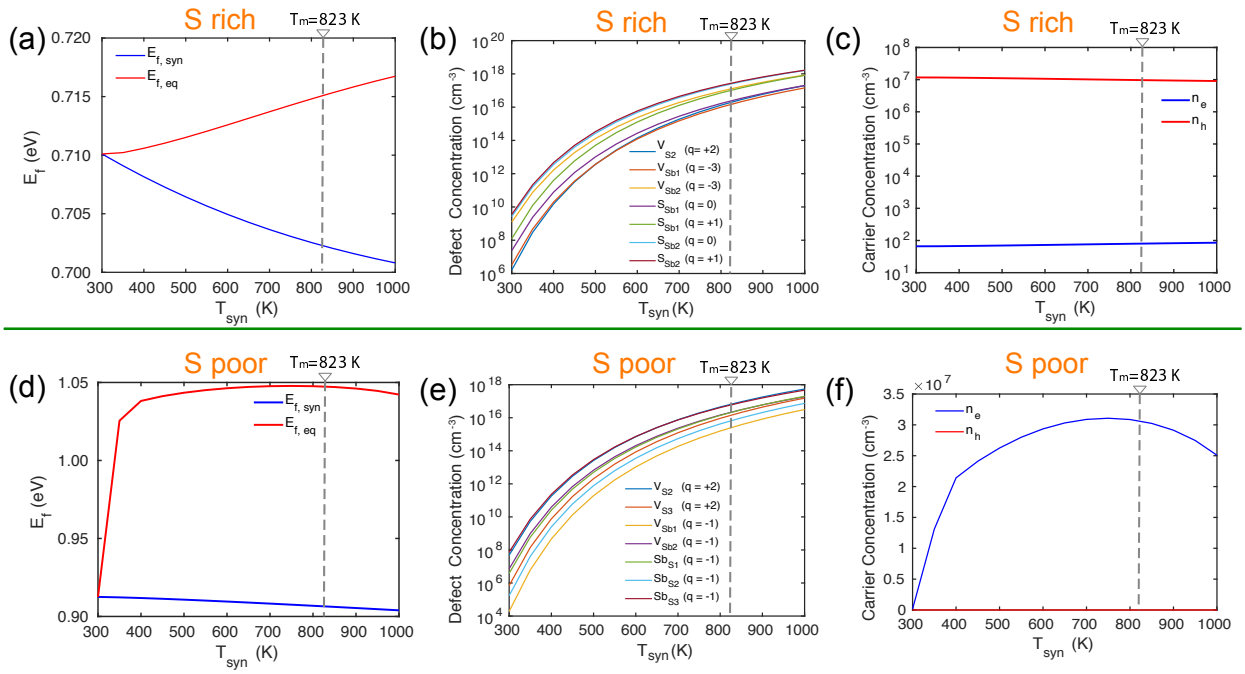

Figure 6. (a) and (c) Fermi level of Sb_2S_3 at synthesis and equilibrium temperatures as a function of synthesis temperature under S rich and S poor conditions, respectively. (b) and (e) Electron and hole densities at equilibrium temperature as a function of synthesis temperature under S rich and S poor conditions, respectively. (c) and (f) The concentration of dominant defects as a function of synthesis temperature under S rich and S poor conditions, respectively. The dashed line indicates the melting temperature of Sb_2S_3 at 823 K.

The same approach was applied to study Sb_2S_3. The results are presented in **Figure 6**. The melting point of Sb_2S_3 is also indicated by dashed line at 823K. In S rich condition, the equilibrium Fermi energy is around 0.7 eV, at which donor defects S_{Sb1}^{+1} and S_{Sb2}^{+1} have high concentrations. However, the acceptor defect V_{Sb2}^{-3} also has high concentration but possesses higher charge state, thereby donating holes to valence bands and leading to the *p*-type in Sb_2S_3 with hole density on the order of 10^7 cm^{-3}. Under S rich condition, the increased concentration of both acceptor (*i.e.*, V_{Sb}) and donor (*i.e.*, S_{Sb}) defects at high temperature competes with each other in Sb_2S_3, resulting in a minimal change in the hole and electron concentration as the temperature increases. The hole concentration slightly decreases and the electron concentration slightly increases as the temperature goes up, as shown in **Figure 6c**. In contrast, Sb_2Se_3 has a more significant variation of the carrier concentration under different synthesis temperature in the Se rich condition, as shown in **Figure 5c**. This is because the concentration of acceptor defects (*i.e.*, Se_{Sb}) increases more significantly than donor defects (*i.e.*, V_{Se}), though both types of defects have higher concentration at high temperature. As a consequence, the concentration of electron carriers contributed by donor defects decreases and the concentration of hole carriers devoted by acceptor defects increases with increasing synthesis temperature in Sb_2Se_3 under Se rich condition (**Figure 5c**). On the other hand, Sb_2S_3 is a weak intrinsic *n*-type under S poor condition, due to the donor defects V_{S2}^{+2} and V_{S3}^{+2}. Such donor defects act as hole killers and reduce the free holes in the material, hence the free hole carrier density is almost negligible (close to 0). As temperature increases, the acceptor defects including V_{Sb2}^{-1}, Sb_{S3}^{-1} and Sb_{S1}^{-1} further overcompensate the donor defects. As a consequence, the free electron has a low density in S poor condition (**Figure 6f**). The Fermi energy is pinned above the mid-gap, as seen in **Figure 6d**, reflecting the *n*-type nature. In general, the carrier density in Sb_2S_3 is significantly lower than that in Sb_2Se_3, which is consistent with experiment findings.

Sb_2Se_3 is intrinsically *p*-type, while Sb_2S_3 is almost intrinsic semiconductor. Further strategies, such as introducing certain dopants, may be conducted to suppress the donor-like defects in order to increase the carrier density.

5. Conclusions

In summary, we systematically investigate the electronic structure and native defects in antimony chalcogenides using first-principles DFT. On one hand, the unique quasi-1D ribbons in Sb_2Se_3 and Sb_2S_3 lead to anisotropic transport with higher group velocity along the ribbon. More importantly, they possess suitable bandgap and high optical absorption that are desirable for photovoltaics. The large Born effective charge and large dielectric constant suggest strong charge screening, thereby reducing carrier scattering and recombination. Besides, the dispersed band structure near VBM and CBM leads to small hole and electron effective masses. The small effective mass and large dielectric constant result in small exciton binding energy, suggesting efficient exciton dissociation and formation of free charge carriers in antimony chalcogenides. Since antimony chalcogenides have soft quasi-1D ribbon-like structures with weak interchain interaction, they are able to accommodate larger lattice relaxation than conventional 3D bulk crystals, thereby exhibiting negative U behavior in these defect structures.

On the other hand, Sb_2Se_3 and Sb_2S_3 exhibit complex defect chemistry competing with the above superior electronic structure of pristine Sb_2Se_3 and Sb_2S_3. The dominating defects include antisite defects, anion vacancies, and interstitial defects. Anion vacancies have low formation energy even under anion-rich condition. The weak vdW interlayer interaction leads to the low formation energy of interstitial defects between Sb_2X_3 ribbons. These defects can create mid-gap transition levels, which may explain the low V_{oc} observed in experiments. In order to improve the V_{oc}, it is necessary to suppress the defects, for example, by optimizing growth condition, post-annealing, or

introducing extrinsic dopant. Regarding the dopability of Sb_2Se_3 and Sb_2S_3, the *p*-type doping for Sb_2Se_3 under Se-rich condition is quite accessible since the pinned Fermi energy is close to VBM, but it will be difficult under Se-poor condition due to the low formation energy of Se vacancies. In contrast, Sb_2S_3 has limited *p*-type and *n*-type dopability under both S-rich and S-poor condition. From the defect concentration and carrier density calculations, we found that Sb_2Se_3 under Se rich condition is *p*-type and the dominant defect is Se_{Sb2} with charge state of -1. Compared to Sb_2Se_3, carrier density in Sb_2S_3 is relatively low, exhibiting intrinsic semiconductor behavior. To suppress the formation of the detrimental defects and increase the absorber layer conductivity, extrinsic doping is a potential strategy. For instance, the introduction of oxygen in Sb_2Se_3 based solar cells can passivate the interfacial diffusion of Cd from the window layer to the absorber layer and the formation of donor defect Cd_i, while O tends to substitute Se in Sb_2Se_3 and form a benign defect without deep level trap state.[51] In a recent theoretical study on Sb_2S_3,[52] Pb and Cl have been proposed as efficient *p*-type and *n*-type dopants, providing a clear guidance for experiments to design high-efficiency antimony chalcogenides based solar cells. An alternative effective approach towards highly defect-tolerant solar absorbers is to form antimony selenosulfide ($Sb_2(S,Se)_3$) alloys, which has recently shown its great potential with a striking efficiency of 10%.[10, 53]

Our present work provided a microscopic understanding of electronic, optical, and dielectric properties of antimony chalcogenides, revealing their great potential for photovoltaic applications as well as the challenges to be addressed, and in particular effort shall be made in future to mitigate the defects and further boost the performance of antimony chalcogenide based solar cells.

ASSOCIATED CONTENT

Supporting Information.

The Supporting Information is available free of charge on the ACS Publications website.

Electronic band structure with and without spin-orbit coupling; defect formation energy correction; lattice constants; band gaps; effective mass of electrons and holes; dielectric constant; exciton binding energy; and Born effective charge of antimony chalcogenides Sb_2Se_3 and Sb_2S_3.

AUTHOR INFORMATION

Corresponding Author

* E-mail: feng@tamu.edu

Author Contributions

X.Q. conceived and supervised the project. B.Z. performed the calculations and developed the code for computing defect and carrier concentration. Both B.Z. and X.Q. analyzed the results and wrote the manuscript.

ACKNOWLEDGMENT

X.Q. acknowledges the support by the US National Science Foundation (NSF) under award number DMR-1753054. B.Z. gratefully acknowledges support from Texas A&M University President's Excellence Fund X-Grants and T3 Program. Portions of this research were conducted with the advanced computing resources provided by Texas A&M High Performance Research Computing.

REFERENCES

(1) Green, M. A.; Hishikawa, Y.; Dunlop, E. D.; Levi, D. H.; Hohl-Ebinger, J.; Ho-Baillie, A. W. Y. Solar cell efficiency tables (version 52). *Progress in Photovoltaics: Research and Applications* **2018,** *26* (7), 427-436, DOI: 10.1002/pip.3040.
(2) Yoshikawa, K.; Kawasaki, H.; Yoshida, W.; Irie, T.; Konishi, K.; Nakano, K.; Uto, T.; Adachi, D.; Kanematsu, M.; Uzu, H.; Yamamoto, K. Silicon heterojunction solar cell with

interdigitated back contacts for a photoconversion efficiency over 26%. *Nature Energy* **2017,** *2*, 17032, DOI: 10.1038/nenergy.2017.32.
(3) Kumar, M.; Dubey, A.; Adhikari, N.; Venkatesan, S.; Qiao, Q. Strategic review of secondary phases, defects and defect-complexes in kesterite CZTS–Se solar cells. *Energy & Environmental Science* **2015,** *8* (11), 3134-3159, DOI: 10.1039/C5EE02153G.
(4) Jung, H. S.; Han, G. S.; Park, N.-G.; Ko, M. J. Flexible Perovskite Solar Cells. *Joule* **2019,** *3* (8), 1850-1880, DOI: 10.1016/j.joule.2019.07.023.
(5) Jeong, M.; Choi, I. W.; Go, E. M.; Cho, Y.; Kim, M.; Lee, B.; Jeong, S.; Jo, Y.; Choi, H. W.; Lee, J.; Bae, J.-H.; Kwak, S. K.; Kim, D. S.; Yang, C. Stable perovskite solar cells with efficiency exceeding 24.8% and 0.3-V voltage loss. *Science* **2020,** *369* (6511), 1615, DOI: 10.1126/science.abb7167.
(6) Kim, K. S.; Zhao, Y.; Jang, H.; Lee, S. Y.; Kim, J. M.; Kim, K. S.; Ahn, J.-H.; Kim, P.; Choi, J.-Y.; Hong, B. H. Large-scale pattern growth of graphene films for stretchable transparent electrodes. *Nature* **2009,** *457* (7230), 706-710.
(7) Zhou, Y.; Wang, L.; Chen, S.; Qin, S.; Liu, X.; Chen, J.; Xue, D.-J.; Luo, M.; Cao, Y.; Cheng, Y.; Sargent, E. H.; Tang, J. Thin-film Sb_2Se_3 photovoltaics with oriented one-dimensional ribbons and benign grain boundaries. *Nat. Photon.* **2015,** *9*, 409, DOI: 10.1038/nphoton.2015.78.
(8) Mavlonov, A.; Razykov, T.; Raziq, F.; Gan, J.; Chantana, J.; Kawano, Y.; Nishimura, T.; Wei, H.; Zakutayev, A.; Minemoto, T.; Zu, X.; Li, S.; Qiao, L. A review of Sb_2Se_3 photovoltaic absorber materials and thin-film solar cells. *Solar Energy* **2020,** *201*, 227-246, DOI: 10.1016/j.solener.2020.03.009.
(9) Li, Z.; Liang, X.; Li, G.; Liu, H.; Zhang, H.; Guo, J.; Chen, J.; Shen, K.; San, X.; Yu, W.; Schropp, R. E. I.; Mai, Y. 9.2%-efficient core-shell structured antimony selenide nanorod array solar cells. *Nat. Commun.* **2019,** *10* (1), 125, DOI: 10.1038/s41467-018-07903-6.
(10) Tang, R.; Wang, X.; Lian, W.; Huang, J.; Wei, Q.; Huang, M.; Yin, Y.; Jiang, C.; Yang, S.; Xing, G.; Chen, S.; Zhu, C.; Hao, X.; Green, M. A.; Chen, T. Hydrothermal deposition of antimony selenosulfide thin films enables solar cells with 10% efficiency. *Nature Energy* **2020,** *5* (8), 587-595, DOI: 10.1038/s41560-020-0652-3.
(11) Huang, M.; Xu, P.; Han, D.; Tang, J.; Chen, S. Complicated and Unconventional Defect Properties of the Quasi-One-Dimensional Photovoltaic Semiconductor Sb_2Se_3. *ACS Applied Materials & Interfaces* **2019,** *11* (17), 15564-15572, DOI: 10.1021/acsami.9b01220.
(12) Liu, X.; Xiao, X.; Yang, Y.; Xue, D.-J.; Li, D.-B.; Chen, C.; Lu, S.; Gao, L.; He, Y.; Beard, M. C.; Wang, G.; Chen, S.; Tang, J. Enhanced Sb_2Se_3 solar cell performance through theory-guided defect control. *Progress in Photovoltaics: Research and Applications* **2017,** *25* (10), 861-870, DOI: 10.1002/pip.2900.
(13) Savory, C. N.; Scanlon, D. O. The complex defect chemistry of antimony selenide. *Journal of Materials Chemistry A* **2019,** *7* (17), 10739-10744.
(14) Hohenberg, P.; Kohn, W. Inhomogeneous Electron Gas. *Physical Review* **1964,** *136* (3B), B864-B871, DOI: 10.1103/PhysRev.136.B864.
(15) Kohn, W.; Sham, L. J. Self-consistent equations including exchange and correlation effects. *Phys. Rev.* **1965,** *140* (4A), A1133-A1138, DOI: 10.1103/PhysRev.140.A1133.
(16) Krukau, A. V.; Vydrov, O. A.; Izmaylov, A. F.; Scuseria, G. E. Influence of the exchange screening parameter on the performance of screened hybrid functionals. *J. Chem. Phys.* **2006,** *125* (22), 224106, DOI: 10.1063/1.2404663.

(17) Grimme, S.; Antony, J.; Ehrlich, S.; Krieg, H. A consistent and accurate ab initio parametrization of density functional dispersion correction (DFT-D) for the 94 elements H-Pu. *The Journal of Chemical Physics* **2010,** *132* (15), 154104, DOI: 10.1063/1.3382344.
(18) Stoliaroff, A.; Lecomte, A.; Rubel, O.; Jobic, S.; Zhang, X.; Latouche, C.; Rocquefelte, X. Deciphering the Role of Key Defects in Sb_2Se_3, a Promising Candidate for Chalcogenide-Based Solar Cells. *ACS Applied Energy Materials* **2020,** *3* (3), 2496-2509, DOI: 10.1021/acsaem.9b02192.
(19) Cai, Z.; Dai, C.-M.; Chen, S. Intrinsic Defect Limit to the Electrical Conductivity and a Two-Step *p*-Type Doping Strategy for Overcoming the Efficiency Bottleneck of Sb_2S_3-Based Solar Cells. *Solar RRL* **2020,** *4* (4), 1900503, DOI: 10.1002/solr.201900503.
(20) Hobson, T. D. C.; Phillips, L. J.; Hutter, O. S.; Durose, K.; Major, J. D. Defect properties of Sb_2Se_3 thin film solar cells and bulk crystals. *Appl. Phys. Lett.* **2020,** *116* (26), 261101, DOI: 10.1063/5.0012697.
(21) Kresse, G.; Furthmüller, J. Efficient iterative schemes for *ab initio* total-energy calculations using a plane-wave basis set. *Physical Review B* **1996,** *54* (16), 11169-11186.
(22) Perdew, J. P.; Burke, K.; Ernzerhof, M. Generalized Gradient Approximation Made Simple. *Physical Review Letters* **1996,** *77* (18), 3865-3868.
(23) Langreth, D. C.; Mehl, M. J. Beyond the local-density approximation in calculations of ground-state electronic properties. *Phys. Rev. B* **1983,** *28* (4), 1809-1834, DOI: 10.1103/PhysRevB.28.1809.
(24) Monkhorst, H. J.; Pack, J. D. Special points for Brillouin-zone integrations. *Physical Review B* **1976,** *13* (12), 5188-5192, DOI: 10.1103/PhysRevB.13.5188.
(25) Becke, A. D.; Johnson, E. R. A simple effective potential for exchange. *The Journal of Chemical Physics* **2006,** *124* (22), 221101, DOI: 10.1063/1.2213970.
(26) Tran, F.; Blaha, P. Accurate Band Gaps of Semiconductors and Insulators with a Semilocal Exchange-Correlation Potential. *Phys. Rev. Lett.* **2009,** *102* (22), 226401.
(27) Goyal, A.; Gorai, P.; Toberer, E. S.; Stevanović, V. First-principles calculation of intrinsic defect chemistry and self-doping in PbTe. *npj Computational Materials* **2017,** *3* (1), 42, DOI: 10.1038/s41524-017-0047-6.
(28) Kumagai, Y.; Tsunoda, N.; Oba, F. Point Defects and *p*-Type Doping in ScN from First Principles. *Physical Review Applied* **2018,** *9* (3), 034019, DOI: 10.1103/PhysRevApplied.9.034019.
(29) Dion, M.; Rydberg, H.; Schröder, E.; Langreth, D. C.; Lundqvist, B. I. Van der Waals Density Functional for General Geometries. *Phys. Rev. Lett.* **2004,** *92* (24), 246401, DOI: 10.1103/PhysRevLett.92.246401.
(30) Klimeš, J.; Bowler, D. R.; Michaelides, A. Van der Waals density functionals applied to solids. *Phys. Rev. B* **2011,** *83* (19), 195131, DOI: 10.1103/PhysRevB.83.195131.
(31) Román-Pérez, G.; Soler, J. M. Efficient Implementation of a van der Waals Density Functional: Application to Double-Wall Carbon Nanotubes. *Phys. Rev. Lett.* **2009,** *103* (9), 096102, DOI: 10.1103/PhysRevLett.103.096102.
(32) Filip, M. R.; Patrick, C. E.; Giustino, F. *GW* quasiparticle band structures of stibnite, antimonselite, bismuthinite, and guanajuatite. *Phys. Rev. B* **2013,** *87* (20), 205125, DOI: 10.1103/PhysRevB.87.205125.
(33) Lardhi, S.; Noureldine, D.; Harb, M.; Ziani, A.; Cavallo, L.; Takanabe, K. Determination of the electronic, dielectric, and optical properties of sillenite $Bi_{12}TiO_{20}$ and perovskite-like

$B_{i4}Ti_3O_{12}$ materials from hybrid first-principle calculations. *J. Chem. Phys.* **2016,** *144* (13), 134702, DOI: 10.1063/1.4945344.
(34) Madelung, O. *Semiconductors: data handbook*, Springer Science & Business Media: 2012.
(35) Young, K. F.; Frederikse, H. P. R. Compilation of the Static Dielectric Constant of Inorganic Solids. *J. Phys. Chem. Ref. Data* **1973,** *2* (2), 313-410, DOI: 10.1063/1.3253121.
(36) Guo, L.; Zhang, B.; Qin, Y.; Li, D.; Li, L.; Qian, X.; Yan, F. Tunable Quasi-One-Dimensional Ribbon Enhanced Light Absorption in Sb_2Se_3 Thin-film Solar Cells Grown by Close-Space Sublimation. *Solar RRL* **2018,** *2* (10), 1800128, DOI: 10.1002/solr.201800128.
(37) Chen, C.; Tang, J. Open-Circuit Voltage Loss of Antimony Chalcogenide Solar Cells: Status, Origin, and Possible Solutions. *ACS Energy Letters* **2020,** *5* (7), 2294-2304, DOI: 10.1021/acsenergylett.0c00940.
(38) Freysoldt, C.; Grabowski, B.; Hickel, T.; Neugebauer, J.; Kresse, G.; Janotti, A.; Van de Walle, C. G. First-principles calculations for point defects in solids. *Rev. Mod. Phys.* **2014,** *86* (1), 253-305, DOI: 10.1103/RevModPhys.86.253.
(39) Broberg, D.; Medasani, B.; Zimmermann, N. E. R.; Yu, G.; Canning, A.; Haranczyk, M.; Asta, M.; Hautier, G. PyCDT: A Python toolkit for modeling point defects in semiconductors and insulators. *Comput. Phys. Commun.* **2018,** *226*, 165-179, DOI: 10.1016/j.cpc.2018.01.004.
(40) Freysoldt, C.; Neugebauer, J.; Van de Walle, C. G. Fully Ab Initio Finite-Size Corrections for Charged-Defect Supercell Calculations. *Phys. Rev. Lett.* **2009,** *102* (1), 016402, DOI: 10.1103/PhysRevLett.102.016402.
(41) Kumagai, Y.; Oba, F. Electrostatics-based finite-size corrections for first-principles point defect calculations. *Phys. Rev. B* **2014,** *89* (19), 195205, DOI: 10.1103/PhysRevB.89.195205.
(42) Oba, F.; Kumagai, Y. Design and exploration of semiconductors from first principles: A review of recent advances. *Applied Physics Express* **2018,** *11* (6), 060101, DOI: 10.7567/apex.11.060101.
(43) Wen, X.; Chen, C.; Lu, S.; Li, K.; Kondrotas, R.; Zhao, Y.; Chen, W.; Gao, L.; Wang, C.; Zhang, J.; Niu, G.; Tang, J. Vapor transport deposition of antimony selenide thin film solar cells with 7.6% efficiency. *Nature Communications* **2018,** *9* (1), 2179, DOI: 10.1038/s41467-018-04634-6.
(44) Lian, W.; Jiang, C.; Yin, Y.; Tang, R.; Li, G.; Zhang, L.; Che, B.; Chen, T. Revealing composition and structure dependent deep-level defect in antimony trisulfide photovoltaics. *Nat. Commun.* **2021,** *12* (1), 3260, DOI: 10.1038/s41467-021-23592-0.
(45) Zunger, A. Practical doping principles. *Appl. Phys. Lett.* **2003,** *83* (1), 57-59, DOI: 10.1063/1.1584074.
(46) Anderson, P. W. Model for the Electronic Structure of Amorphous Semiconductors. *Phys. Rev. Lett.* **1975,** *34* (15), 953-955, DOI: 10.1103/PhysRevLett.34.953.
(47) Yan, Q.; Janotti, A.; Scheffler, M.; Van de Walle, C. G. Role of nitrogen vacancies in the luminescence of Mg-doped GaN. *Appl. Phys. Lett.* **2012,** *100* (14), 142110, DOI: 10.1063/1.3699009.
(48) Tang, W.; Sanville, E.; Henkelman, G. A grid-based Bader analysis algorithm without lattice bias. *J. Phys. Condens. Matter* **2009,** *21* (8), 084204, DOI: 10.1088/0953-8984/21/8/084204.
(49) Sun, R.; Chan, M. K. Y.; Kang, S.; Ceder, G. Intrinsic stoichiometry and oxygen-induced *p*-type conductivity of pyrite FeS_2. *Phys. Rev. B* **2011,** *84* (3), 035212, DOI: 10.1103/PhysRevB.84.035212.

(50) Krautmann, R.; Spalatu, N.; Gunder, R.; Abou-Ras, D.; Unold, T.; Schorr, S.; Krunks, M.; Oja Acik, I. Analysis of grain orientation and defects in Sb_2Se_3 solar cells fabricated by close-spaced sublimation. *Solar Energy* **2021,** *225*, 494-500, DOI: 10.1016/j.solener.2021.07.022.
(51) Guo, L.; Zhang, B.; Ranjit, S.; Wall, J.; Saurav, S.; Hauser, A. J.; Xing, G.; Li, L.; Qian, X.; Yan, F. Interface Engineering via Sputtered Oxygenated CdS:O Window Layer for Highly Efficient Sb_2Se_3 Thin-Film Solar Cells with Efficiency Above 7%. *Solar RRL* **2019,** *3* (10), 1900225, DOI: 10.1002/solr.201900225.
(52) Cai, Z.; Chen, S. Extrinsic dopants in quasi-one-dimensional photovoltaic semiconductor Sb_2S_3: A first-principles study. *J. Appl. Phys.* **2020,** *127* (18), 183101, DOI: 10.1063/1.5140751.
(53) Huang, M.; Cai, Z.; Chen, S. Quasi-one-dimensional $Sb_2(S,Se)_3$ alloys as bandgap-tunable and defect-tolerant photocatalytic semiconductors. *J. Chem. Phys.* **2020,** *153* (1), 014703, DOI: 10.1063/5.0013217.

Table of Content

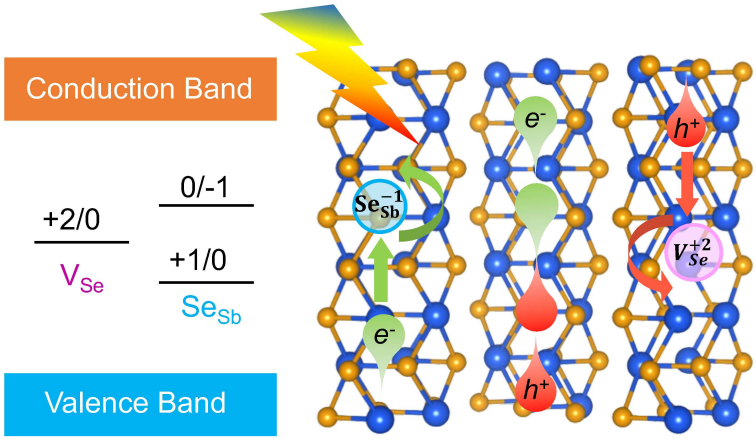

Supporting Information

Competing Superior Electronic Structure and Complex Defect Chemistry in Quasi-One-Dimensional Antimony Chalcogenide Photovoltaic Absorbers

Baiyu Zhang[1] *and Xiaofeng Qian*[1,2,*]

1. Department of Materials Science and Engineering, Texas A&M University, College Station, Texas, 77843, USA

2. Department of Electrical and Computer Engineering, Texas A&M University, College Station, Texas, 77843, USA

*Corresponding Author: feng@tamu.edu (X.Q.)

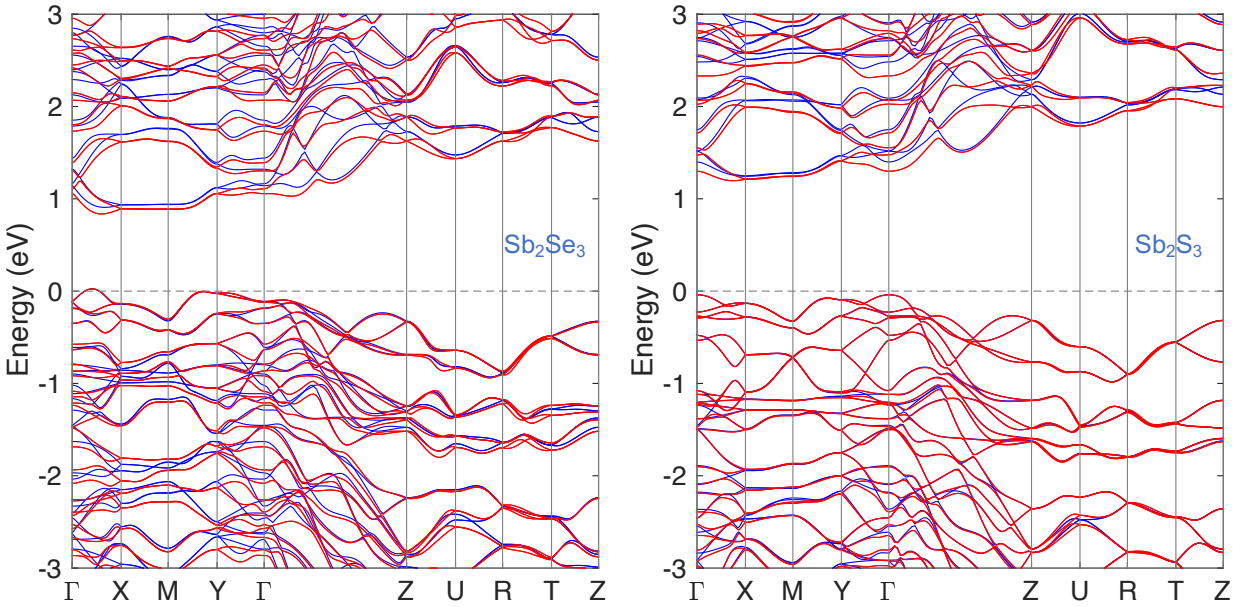

Figure S1. Electronic band structures of Sb_2Se_3 and Sb_2S_3 with (red) and without (blue) spin-orbit coupling (SOC). Different from many perovskites, such as $CsPbBr_3$ and $CsPbI_3$ where SOC can induce the bandgap change as large as 1 eV, the impact of SOC on the band structures of Sb_2Se_3 and Sb_2S_3 is much smaller, particularly at the band edges.

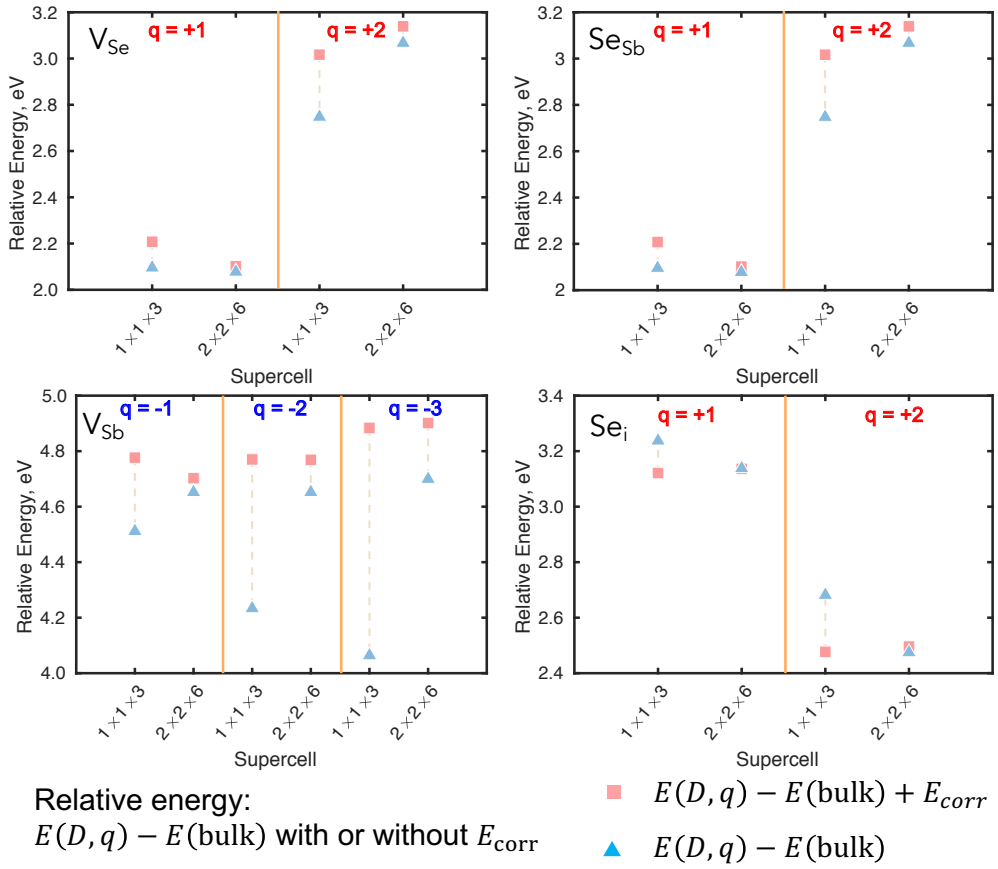

Figure S2. Comparison of the relative energies for charged defects V_{Se}, Se_{Sb}, V_{Sb}, and Se_i in Sb_2Se_3 in 1×1×3 and 2×2×6 supercells with and without energy correction. The pink square and blue triangle symbols indicate the relative energies with and without the finite size correction, respectively. The finite size correction in defect formation energy calculations for charged defects is based on the method by Oba and Kumagai.[1] It addresses two issues: the potential alignment between the pristine bulk and defect supercell, and the interaction between the defect charge and its periodic images. This correction term plays a critical role in determining the defect formation energy in the dilute limit, as the relative energies with and without the correction differ significantly, especially in a small supercell of 1×1×3. The relative energies with the correction of 1×1×3 are close to those in the dilute limit with a supercell size of 2×2×6, showing this correction scheme successfully corrected the formation energy.

Table S1. Lattice constants of Sb_2Se_3 and Sb_2S_3 in Pnma (#62) space group calculated by DFT with different exchange-correlation energy functionals.

		Sb_2Se_3			Sb_2S_3		
lattice parameters		a	b	c	a	b	c
DFT	PBE+vdW-optB86	11.45	11.89	4.01	11.06	11.32	3.86
	PBE+ vdW-D3	11.48	12.02	4.02	11.11	11.43	3.86
	HSE06+ vdW-optB86	11.95	12.26	4.01	11.66	11.51	3.85
	HSE06+ vdW-D3	11.50	11.96	3.95	11.17	11.42	3.80
Exp.[2-3]		11.62	11.77	3.96	11.23	11.31	3.84

Table S2. Calculated band gaps of Sb_2Se_3 and Sb_2S_3 using different exchange-correlation functionals.

		Direct gap (eV)	Indirect gap (eV)
Sb_2Se_3	Exp.[4]	1.20	1.15
	DFT-HSE06	1.43	1.39
	DFT-MBJ	1.38	1.35
Sb_2S_3	Exp.[5]	1.71	1.56
	DFT-HSE06	1.93	1.79
	DFT-MBJ	1.90	1.79

Table S3. Anisotropic effective mass and exciton binding energy in Sb_2Se_3. In general, Sb_2Se_3 has small effective hole mass, which is desirable for *p*-type semiconductors. Their binding energies are also very small, comparable to the thermal energy at room temperature (k_BT, ~ 26 meV).

	m_h (m_0)	m_e (m_0)	μ (m_0)	ε_{elec}	E_b (meV)
xx	0.42	17.51	0.41	15.43	23.4
yy	0.83	0.98	0.45	10.69	53.5
zz	0.52	0.40	0.23	15.46	12.9

Table S4. Anisotropic effective mass and exciton binding energy in Sb_2S_3. In general, Sb_2S_3 has small effective hole mass, and relatively large effective electron mass, which is desirable for *p*-type semiconductors. Their binding energies are still small, though larger than those in Sb_2Se_3.

	m_h (m_0)	m_e (m_0)	μ (m_0)	ε_{elec}	E_b (meV)
xx	0.56	1.62	0.42	11.06	46.3
yy	0.80	6.45	0.53	8.28	141.2
zz	0.41	8.69	0.39	11.63	39.4

Table S5. Born effective charge for symmetry-inequivalent atoms from DFT-PBE calculations.

	Ion	Z_{xx}	Z_{xy}	Z_{xz}	Z_{yx}	Z_{yy}	Z_{yz}	Z_{zx}	Z_{zy}	Z_{zz}
Sb_2Se_3	*Sb1*	4.38	0.00	0.00	0.44	2.63	0.00	0.00	0.00	7.22
	Sb2	7.49	-1.86	0.00	-0.19	2.15	0.00	0.00	0.00	5.80
	Se1	-4.19	-1.19	0.00	-1.04	-1.76	0.00	0.00	0.00	-4.08
	Se2	-3.33	1.51	0.00	0.03	-1.58	0.00	0.00	0.00	-4.01
	Se3	-4.35	-0.06	0.00	-0.18	-1.44	0.00	0.00	000	-4.93
Sb_2S_3	*Sb1*	3.95	0.35	0.00	0.27	2.83	0.00	0.00	0.00	6.86
	Sb2	6.38	-1.47	0.00	0.01	1.96	0.00	0.00	0.00	5.36
	S1	-3.44	-0.83	0.00	-0.84	-2.00	0.00	0.00	0.00	-3.86
	S2	-3.24	1.28	0.00	-0.05	-1.39	0.00	0.00	0.00	-3.75
	S3	-3.65	0.35	0.00	0.37	-1.39	0.00	0.00	0.00	-4.59

References

(1) Kumagai, Y.; Oba, F. Electrostatics-based finite-size corrections for first-principles point defect calculations. *Phys. Rev. B* **2014,** *89* (19), 195205, DOI: 10.1103/PhysRevB.89.195205.

(2) Tideswell, N.; Kruse, F.; McCullough, J. The crystal structure of antimony selenide, Sb_2Se_3. *Acta Crystallographica* **1957,** *10* (2), 99-102.

(3) Kyono, A.; Kimata, M.; Matsuhisa, M.; Miyashita, Y.; Okamoto, K. Low-temperature crystal structures of stibnite implying orbital overlap of Sb $5s^2$ inert pair electrons. *Physics and Chemistry of Minerals* **2002,** *29* (4), 254-260, DOI: 10.1007/s00269-001-0227-1.

(4) Guo, L.; Zhang, B.; Qin, Y.; Li, D.; Li, L.; Qian, X.; Yan, F. Tunable Quasi-One-Dimensional Ribbon Enhanced Light Absorption in Sb_2Se_3 Thin-film Solar Cells Grown by Close-Space Sublimation. *Solar RRL* **2018,** *2* (10), 1800128, DOI: 10.1002/solr.201800128.

(5) Guo, L.; Zhang, B.; Li, S.; Zhang, Q.; Buettner, M.; Li, L.; Qian, X.; Yan, F. Scalable and efficient Sb_2S_3 thin-film solar cells fabricated by close space sublimation. *APL Materials* **2019,** *7* (4), 041105, DOI: 10.1063/1.5090773.